

A LAMINAR TAILORED WING WITH CATNLF AND HLFC FOR EXTRA LONG RANGE

Javier Ruberte Bailo[1], Thomas Streit[1] & Arne Seitz[1]

[1]German Aerospace Center (DLR), Lilienthalplatz 7, Braunschweig, 38108, Germany

Abstract

A Natural Laminar Flow (NLF) and Hybrid Laminar Flow (HLFC), backward swept wing (BSW) with a lift coefficient of 0.52, a wingspan of 63.86 meters and an aspect ratio of 11.74 for a Reynolds number of 30.2 Million and a Mach number of 0.83 has been developed during the Laminar Tailored Aircraft (LamTA) project. Starting from a conceptual design, a reference lift distribution, a thickness distribution, and a detailed turbulent design was developed, which was then further developed into a HLFC Aircraft with NLF on the outer wing. A glide ratio of 25.64 was achieved with the turbulent reference which has been further improved to 28.33 by implementing laminar flow. In order to achieve laminar flow on the configuration, Crossflow Attenuated Natural Laminar Flow (CATNLF) profiles were designed in wingspan region between 44% and 85% span which enabled to achieve NLF up to 60% span, in order to achieve a laminar boundary layer further inward, HLFC was used. The configuration has been designed using the DLR in-house inverse design code and the stability analysis coco/lilo. The post processing of the geometries has been done with the in-house software WiBoDra

Keywords: Long range transport aircraft, Natural Laminar Flow, CATNLF, Inverse design methods

1. Nomenclature

ALT	Attachment line transition
AR	Aspect ratio
b	Span [m]
BM	Bending moment [Nm]
BSW	Backward swept wing
c	chord
CATNLF	Crossflow attenuated natural laminar flow
CF, CFI	Cross flow, cross flow instabilities
C_L,C_D	Lift and drag coefficient
C_{Dpv}	viscous induced pressure drag coefficient
C_{Df},C_{Dw},C_{Di}	friction, wave and induced drag coefficient
C_P	Pressure coefficient
C_x	Force coefficient in the *x* direction
C_y	Force coefficient in the *y* direction
d.c.	Drag counts 0,001 C_D
$E = C_L/C_D$	Glide ratio
E_{FLWR}	Flower Glide ratio, missing fuselage viscous drag
η	relative position along the wingspan
h	height
HLFC	Hybrid Laminar Flow Control

HS	High speed
κ_A	technology factor
kW	Kilowatts
m	mass [T]
Ma	Mach number
MAC	Mean aerodynamic chord
Ma_{DD}	Divergence Mach number
NLF	Natural laminar flow
ϕ, ϕ_{eff}	Geometrical and effective sweep angle
Re	Reynolds number
S	Surface [m^2]
t	Absolute thickness
t/c	Relative thickness
TS, TSI	Tollmien-Schlichting, Tollmien-Schlichting instabilities
x, z, y	Aircraft fixed coordinate system
xle, xte	x position of the leading and trailing edge
xtru	x position of the transition on the upper side of the wing

2. Introduction

Reduction of greenhouse emissions is and has been for a long time a strong motivation for the aerospace industry. Different approaches might be used to achieve such a goal, one of them is to improve the aerodynamic efficiency by utilization of laminar flow wings and therefore by reducing the viscous drag.

Previous work has been already published for a medium range aircraft with a backward swept wing by the authors regarding NLF at high Reynolds numbers and moderate levels of wing sweep by implementing CATNLF for the inner wing [1]. For a long-range aircraft with larger Reynolds number and larger leading-edge sweep, transition due to crossflow and attachment line transition occurs early, which makes the implementation of laminar flow increasingly more difficult. In the previous long-range aircraft project (HLFC-Win) laminar flow was achieved using hybrid boundary layer suction (HLFC) [2], however the suction system adds system complexity. The goal of LamTA in this regard is to achieve as much natural laminar flow as feasible with CATNLF and apply HLFC only in the regions of the wing where laminar flow can not be achieved by passive means.

By introducing CATNLF Campbell and Lynde have already shown that it is possible to achieve natural laminar flow at the flow conditions necessary for a long range aircraft [3] [4]. Furthermore, Tokugawa [5] has demonstrated that natural laminar flow can be achieved in a vertical tail plane at very challenging conditions, with a leading edge sweep of 40 degrees and a Reynolds number of 32 Million at the mean aerodynamic chord.

The focus of the current paper is providing a reference turbulent geometry and the constraints for the laminar design. In addition, the improvements that have been achieved through laminarization during the LamTA project are described. The turbulent geometry has been developed as a previous step towards the laminar geometry. Some insight in further development towards laminar flow in long range aircraft in DLR will also be presented. The goal of the design of the turbulent geometry is to provide a baseline from which the laminar geometry can be further developed, by comparing both geometries the advantages of laminar flow can be evaluated whereas other performance improvements coming from planform, lift distribution or relative thickness can be disregarded.

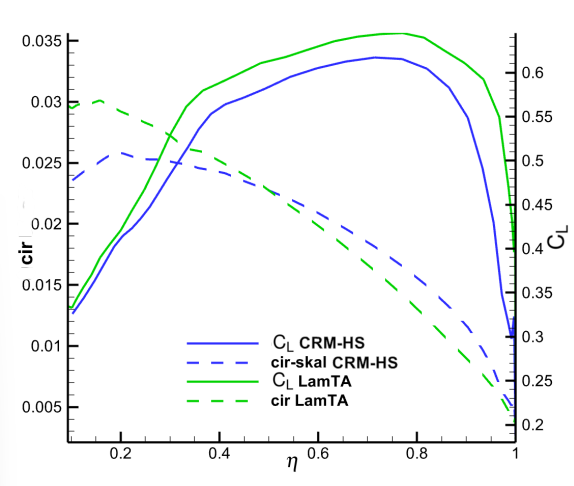
3. Methodology

The wing was designed using the 3D DLR transonic inverse design code implemented in the CFD code FLOWer [6] and a drag breakdown has been obtained with the DLR near field postprocessing tool Wing Body Drag Breakdown (WiBoDra) [7] which provides global and local aerodynamic coefficients and forces. Additionally geometrical wing parameters which characterize the wing are given. Altogether this information is useful for improving and assessing the design.

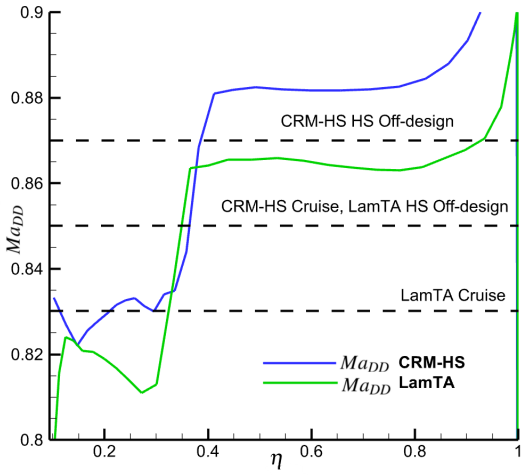
The RANS simulations of the wing-body configuration have been obtained with the DLR CFD solver FLOWer, and the e^N transition module coco and lilo [8]. The meshes are CH-structured, with the wing

Geometry overview / Reference values									
Name	Mach	MAC (m)	Re (1e6)	h (FL)	S (m^2)	C_L	b (m)	AR	m (T)
LamTA	0.83	5.07	30.2	FL370	323.9	0.52	63.86	11.74	359.12
oLAF	0.83	7.58	49.0	FL350	337.0	0.477	58.86	10.28	377.18
CRM – HS	0.85	7.0	40.0	FL385	383.7	0.50	58.76	9.0	428.96
CRM – NLF	0.85	7.0	30.0	FL445	383.7	0.50	58.76	9.0	299.13

Table 1 – Most important characteristics of the considered geometries



(a) Wingspan distributions of lift coefficient and circulation. Circulation has been scaled with weight, square of speed and surface differences between CRM-HS and LamTA



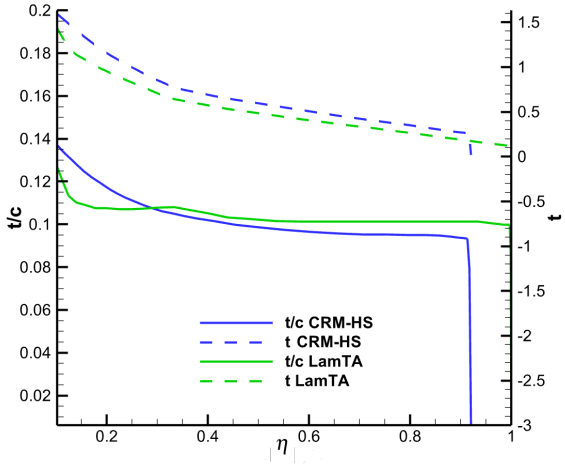
(b) Wingspan distribution of Ma_{DD} calculated with the Korn eqn. using the same technology factor of 0.95

Figure 1 – Wingspan distributions of lift and drag divergence Mach number in LamTA

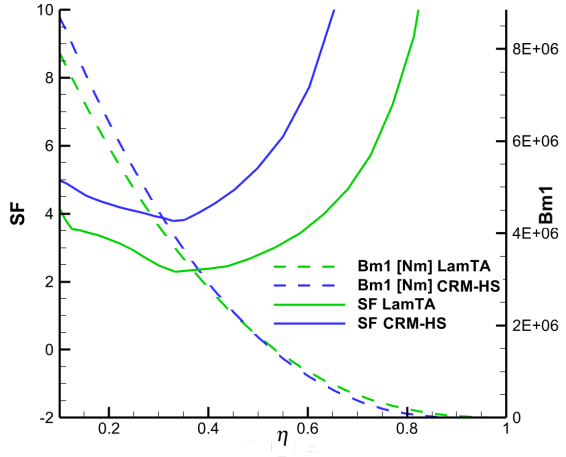
having 33 planes in the wingspan direction and 321 points around the chord. The Fuselage is handled as a inviscid wall (Euler). Further insights of the meshes have been published in [7]. The accuracy of the mesh has been proved to be at comparable level of accuracy with a 20 million unstructured grid at a previous project, ULTIMATE [1], while the used structured wind body mesh requires less computational effort for the CFD solution. The quick turnaround is very useful for the design task, which requires a large number of CFD solutions. Along the development, different snapshots of the geometry have been cross-checked with the DLR TAU RANS code [9].

Starting from a previous project of DLR, oLAF [10], a preliminary design was performed [11] which then was aerodynamically and structurally developed to become the turbulent reference geometry. Further structure insights have been already published by Schulze [12]. The NASA CRM-HS [13] and the NASA CRM-NLF [14] have been used as a reference. Table 1 shows an overview of the different geometries. For both LamTA and the oLAF configuration there has been a mission planning, therefore, a flight level height (FL) and an aircraft mass have been defined. They just provide a background for the used aerodynamic values. Also for the CRM-HS and the CRM-NLF geometries, a FL has been obtained which provides the atmospheric properties in order to achieve the defined Reynolds numbers. The obtained flight level of the NASA CRM-NLF is significantly higher than the others, since it was derived from the CRM-HS but the Reynolds number was kept at 30 Million in order to develop a proof-of-concept wind-tunnel geometry.

Table 2 shows the performance of the different references, all results consider a wing-body configuration without engine. The results for the oLAF reference have been obtained from a wing-body-nacelle configuration, the additional drag due to the nacelle has been taken to be 25 d.c. Due to the methodology used, the viscous drag of the fuselage has to be considered in order to achieve the proper glide ratio. The corrected values of the glide ratio have been achieved by cross-checking the ge-



(a) Wingspan distributions of relative and absolute thickness. Wingspan has been scaled according to LamTA's Wingspan, therefore, CRM-HS's wingspan is only 92% of LamTA's wingspan



(b) Wingspan distribution of bending moment and safety factor for CRM-HS and LamTA. Wingspan has been scaled according to LamTA's Wingspan, therefore, CRM-HS's wingspan is only 92% of LamTA's wingspan

Figure 2 – Representation of the thickness, the bending moment and the safety factor along the wingspan in LamTA

RANS performance metrics								
Name	C_L	C_D	C_{Dpv}	C_{Df}	C_{Dw}	C_{Di}	E_{FLWR}	E
LamTA Turbulent	0.52	0.0161	38.3	39.8	3.3	79.6	32.35	25.64
LamTA Laminar	0.52	0.0142	24.6	24.9	14.8	77.7	36.74	28.33
oLAF	0.477	0.0235*	-	-	-	-	-	20.29
$CRM-HS$	0.499	0.0178	49.0	38.9	1.2	88.9	29.29	22.69
$CRM-NLF(Lam)$**	0.5	0.0220	-	-	-	-	-	22.72
$CRM-NLF(Tur)$**	0.5	0.0246	-	-	-	-	-	20.32

Table 2 – RANS performance metrics for laminar and turbulent flow, *oLAF configuration has also the fuselage friction drag, **Values taken from [14]

ometries with TAU RANS calculations which takes into consideration also the fuselage viscous drag. For the CRM-NLF configuration the available values published by [14] have been used, which were backed up by the authors of [15]. Due to similar Reynolds numbers, a similar drag reduction of 26 d.c. through laminar flow was targeted in LamTA. The viscous drag provided by the TAU solutions for the fuselage is 42 d.c. This value has been used to calculate E from E_{FLWR} for the FLOWer calculations.

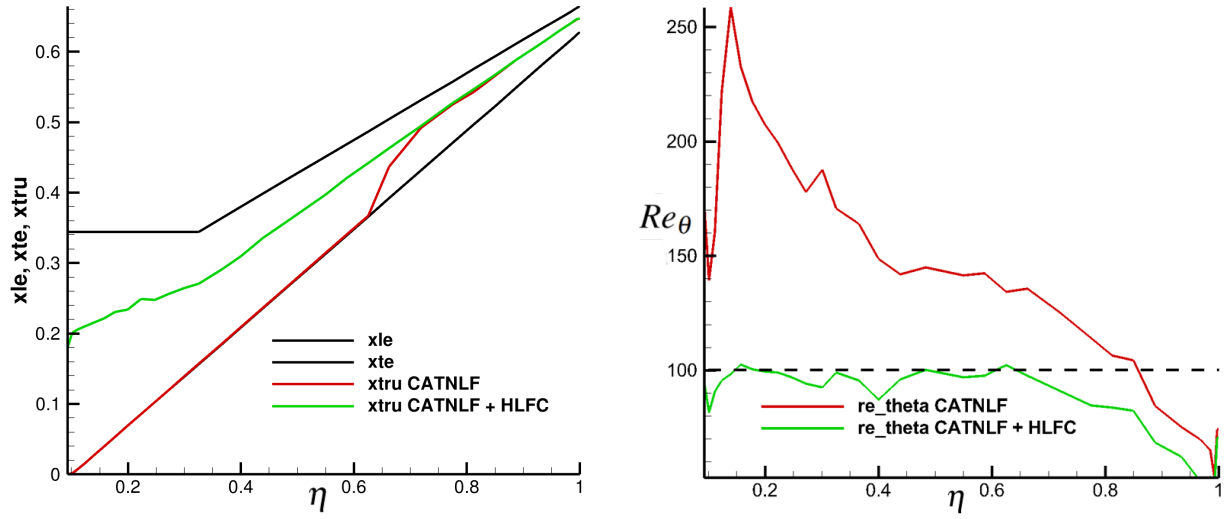
4. Reference geometries overview

The higher AR present in the LamTA configuration provides a challenge with regards to a proper lift distribution concerning induced drag which at the same time does not compromise on structural weight. On the other hand, higher AR leads to lower Reynolds number which makes the implementation of laminar flow easier. In order to achieve such a lift distribution, the CRM-HS configuration was used as a reference.

Figure 1 and Figure 2 show an overview of the most important parameters considered while designing the LamTA configuration. Figure 1a shows the lift and circulation distribution, fig. 1b shows the divergence Mach number calculated with the Korn equation 1 and a technology factor κ_A of 0.95.

$$Ma_{DD} + \frac{C_L}{10} + \frac{t}{c} = \kappa_A \tag{1}$$

Figure 2a shows the relative and the absolute thickness and 2b shows the absolute bending moment of the wing on cruise flight, additionally a safety factor has been calculated, for which an rough



(a) Laminar extent for CATNLF and CATNLF + HLFC

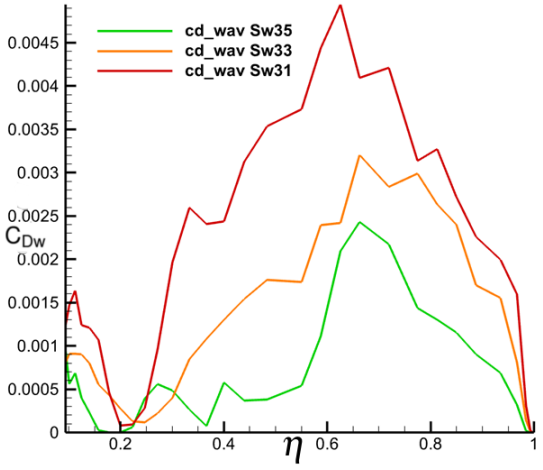
(b) Wingspan distributions of Re_θ for CATNLF and CATNLF + HLFC

Figure 3 – Representation of the CATNLF and CATNLF + HLFC Laminar extent in LamTA

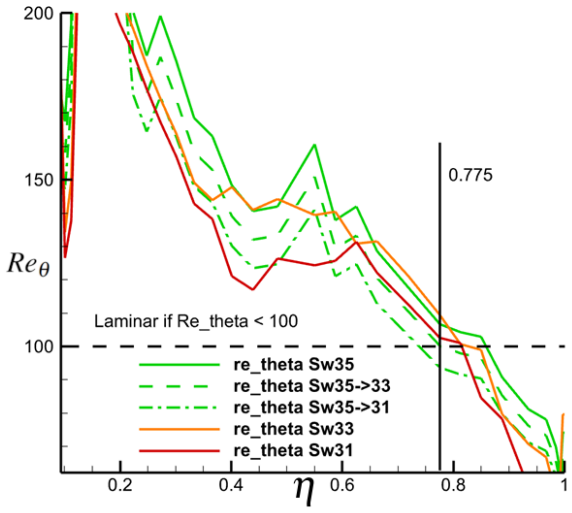
estimation is made considering absolute values of aerodynamic bending moment, cross-sectional moment of inertia, and tensile strength of black aluminium. The wing box is assumed to be a rectangle with a base from 20% to 60% chord length and a height as the absolute thickness at 60% chord. The published values of safety factor are just a reference value which compares the local bending moment to the ultimate strength of a simple structure based in the geometry of the wing. This model is intended to give the aerodynamic designer structure insights when comparing different wings.
As figure 1b shows, both the CRM-HS and the LamTA configurations have similar values of Mach divergence numbers along the wingspan with regard to each other's cruise Mach number. There is an offset between the two configurations which is close to the offset obtained in cruise Mach number. Figures 1a, and 2a show the main differences between the CRM-HS and the LamTA configurations, which are a result from LamTA having a higher AR. The CRM-HS configuration has a more elliptical circulation with lower values of local lift. Furthermore, the CRM-HS configuration has lower relative thickness along most of the wing while the absolute thickness is kept above the absolute thickness of LamTA.
Despite having a smaller wingspan, in fig. 2b can be observed that from 50% onwards, the CRM-HS has higher bending moment than LamTA. Nevertheless, due to the bigger absolute thickness of the CRM-HS, the safety factor of the LamTA configuration is lower, which hints that the structure in LamTA would be heavier than the CRM-HS.
The performance achieved by LamTA as well as the calculated references and the drag breakdown obtained with WiBoDra is shown in table 2. The LamTA configuration shows an overall reduction of the induced drag and viscous induced pressure drag, which translates to a much-improved overall performance. For the turbulent LamTA configuration, the friction drag is close to the one found in the CRM-HS configuration. The improvement through laminarization will be discussed on the next section.

5. Results

Due to the high Reynolds number and the high leading-edge sweep, achieving laminar flow is not an easy task. Figure 7 which is based on [16], shows that the LamTA configuration on the outer wing is as challenging as the NASA CRM-NLF [14], on the other hand the inner wing is deep in high Reynolds numbers, which would be usually considered only to be laminarized with HLFC. The main difference between the laminar approach of DLR and NASA is the incompressible versus compressible stability analysis. While NASA uses compressible stability analysis, DLR uses incompressible



(a) Wingspan distribution of wave drag for three geometries with varying leading-edge sweep



(b) Wingspan distributions of Re_θ for three geometries with varying leading-edge sweep and two calculated distributions with 3 originating from 35° and calculated for 33° and 31°

Figure 4 – Representation of the effects of LE sweep on wave drag and ALT, Three LE Sweeps have been assessed the original 35° and two lower ones of 33° and 31°

stability analysis which is also more pessimistic and therefore, requires the usage of HLFC for the inner wing. Further comparison between both methodologies applied for the CRM-NLF geometry can be found in [17].

Figure 3a shows the extent of laminarity achieved with CATNLF and CATNLF and HLFC. The laminar extent achieved though CATNLF goes from the wing tip up to 65% span, with a maximum chord Reynolds number of 21.9 Million. Attachment line transition may occur due to contamination for Re_θ higher than 100. Although Attachment line transition does not occur for larger Re_θ values in the absence of contamination, with higher values of Re_θ than 100, oncoming turbulence would limit the laminar extent to 85% of the span and outwards. Re_θ is calculated with the following equation where Θ^* is equal to 0.4044 for NLF.

$$\overline{Re} = \left(\frac{Q_\infty r}{\nu} \frac{sin\varphi \quad tan\varphi}{2} \right) \tag{2}$$

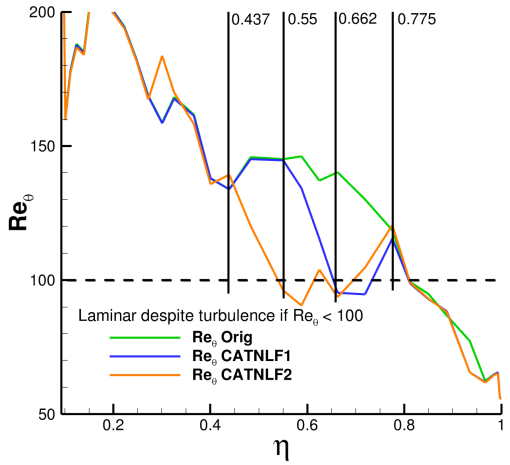
$$Re_\theta = \Theta^* \quad \overline{Re} \tag{3}$$

Due to the proximity of the fuselage, the inner wing has a much higher risk of attachment line transition due to contamination than the outboard wing. Assuming no oncoming contamination and choosing Re_θ = 150, Fig. 3a shows that the possible spanwise extent of laminar flow without attachment line transition increases to a region going from 45% and beyond. The Re_θ values along the wingspan are shown in Fig. 3b. In subsection 5.2 it is shown which values of Re_θ have been achieved in LamTA trough CATNLF.

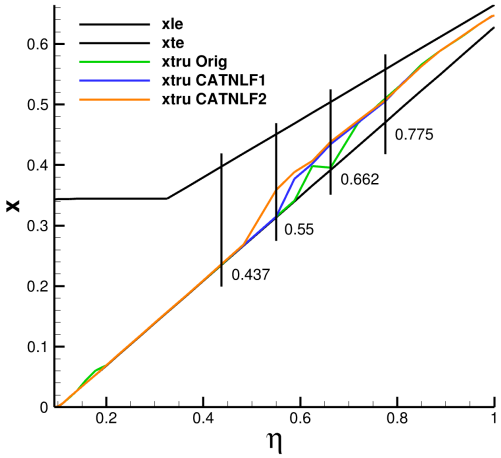
The CATNLF and HLFC configuration shows as displayed in table 2 a reduction of friction drag of 14.9 drag counts and a reduction of viscous induced pressure drag of 13.7 drag counts which elevates the glide ratio from the 25.64 obtained with the turbulent configuration to 28.33. Although the overall performance is very good, detailed shape design work is still ongoing. The wave drag has increased 11.5 drag counts and should be considered in further designs. Additionally, as previously discussed, there is still some performance to be achieved though CATNLF.

5.1 Sweep effect on transition

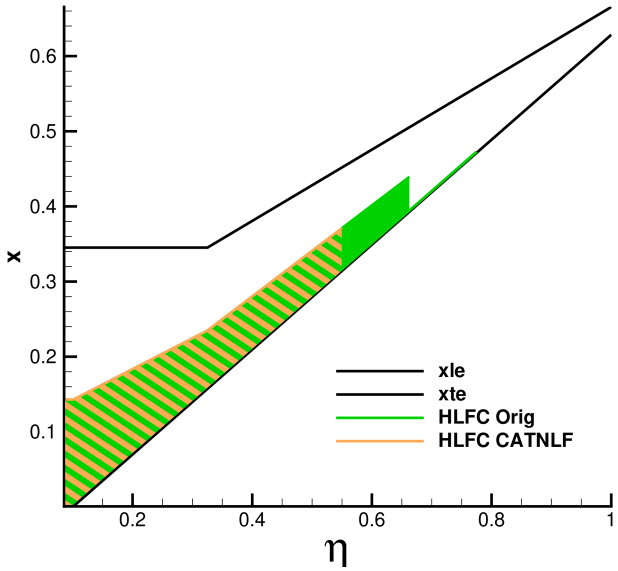
In the past, many work has been done for turbulent airfoils to quantify performance. One of the most known examples of this is the Korn equation and a technology factor for a given airfoil design



(a) Wingspan distribution of Re_θ for a CATNLF study, Re_θ gets substantially reduced by exchanging the airfoil found at η = 0.662 and η = 0.55 by an airfoils with a stronger CATNLF gradient

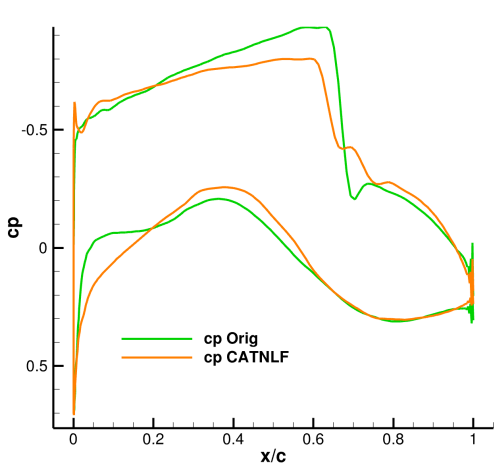


(b) Laminar extent for a CATNLF study, laminar extent increase through CATNLF allowing to limit the HLFC suction to the inner wing up to η = 0.5

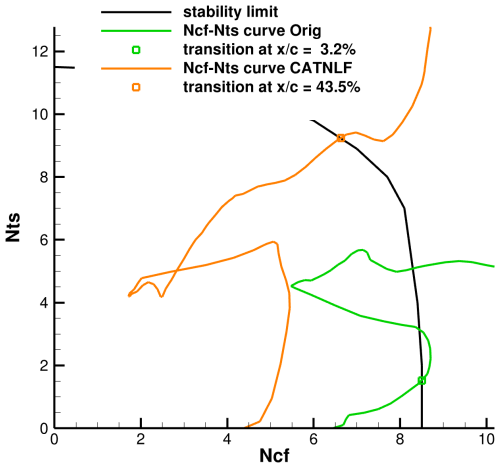


(c) Representation of the reduction of the HLFC extent achieved through CATNLF

Figure 5 – Representation of the effects of CATNLF airfoils in values of Re_θ, laminar extent and HLFC extension



(a) Pressure distribution at η = 0.662. The stronger CATNLF gradient leads to lower Re_θ values and the adverse pressure gradient at the leading edge reduces the Ncf values



(b) Nts and Ncf curve at η = 0.662. The stronger CATNLF gradient and the adverse pressure gradient at the leading edge reduce the crossflow N-factor to a minimum value of 2, which allows for further laminar length

Figure 6 – Representation of pressure distribution and N-factors for the original geometry and a geometry with stronger, CATNLF gradients. Local Reynolds number 19.62 Million

strategy. Due to the novelty of CATNLF airfoils it is difficult to assess in which way should a wing which is intended to be designed with CATNLF profiles be designed. The current planform is heavily based in the turbulent configuration oLAF, therefore a leading edge (LE) sweep of 35 degrees was chosen for the cruise Mach of 0.83. Some efforts have been focused in assessing how much a 3d laminar wing can benefit of a lower LE sweep. For a NLF configuration, a LE sweep of 33 and 31 degrees were tested. The results showed, that as it was expected, the Re_θ values go down and the wave drag goes up with lower sweep, but assessing which LE sweep is optimal in terms of a compromise between laminarity and wave drag is not an easy task.
The results obtained can be observed in fig. 4. Figure 4a shows the increase of wave drag as the sweep decreases. Figure 4b shows the effect of wing sweep in Re_θ for three geometries (solid lines) and the expected values derived from the original 35° LE sweep geometry with the Re_θ equation 3 (dash and dash-point lines).
Although according to the equation 3 the Re_θ values can be reduced with lower LE sweep, the real geometry shows that due to the complexity of a 3d wing, some regions of the wing can overshoot the expected improvement on Re_θ while other regions can even get worse.

5.2 Further potential of CATNLF

Due to time constraints and availability of HLFC in the LamTA project it was decided that values of 150 of Re_θ were enough. Furthermore, beyond the contamination threshold of Re_θ = 100, without contamination, attachment line transition may not occur up to approximately Re_θ = 230. Stronger CATNLF gradients allow for more laminarity and better values of Re_θ, although $C_{L\ MAX}$ and available space for high lift devices can be compromised. On the other hand, allowing higher values of Re_θ can lead to unexpected transition due to oncoming turbulence, therefore for such a design HLFC on the attachment line region would be needed. In order to observe what kind of improvements can be obtained through CATNLF, a test was carried out, in which the final LamTA geometry was updated with profiles with a stronger CATNLF gradients at η positions of 0.66 and 0.55.
Figure 5a shows how the stronger CATNLF gradient leads to a reduction of Re_θ in a large region. Laminarity was also improved in the adjacent region. Due to the introduction of stronger CATNLF, the outer wing has become fully NLF which allows to reduce the system complexity, the weight and the power consumption of the HLFC system from 56.1kW to 36.9kW.

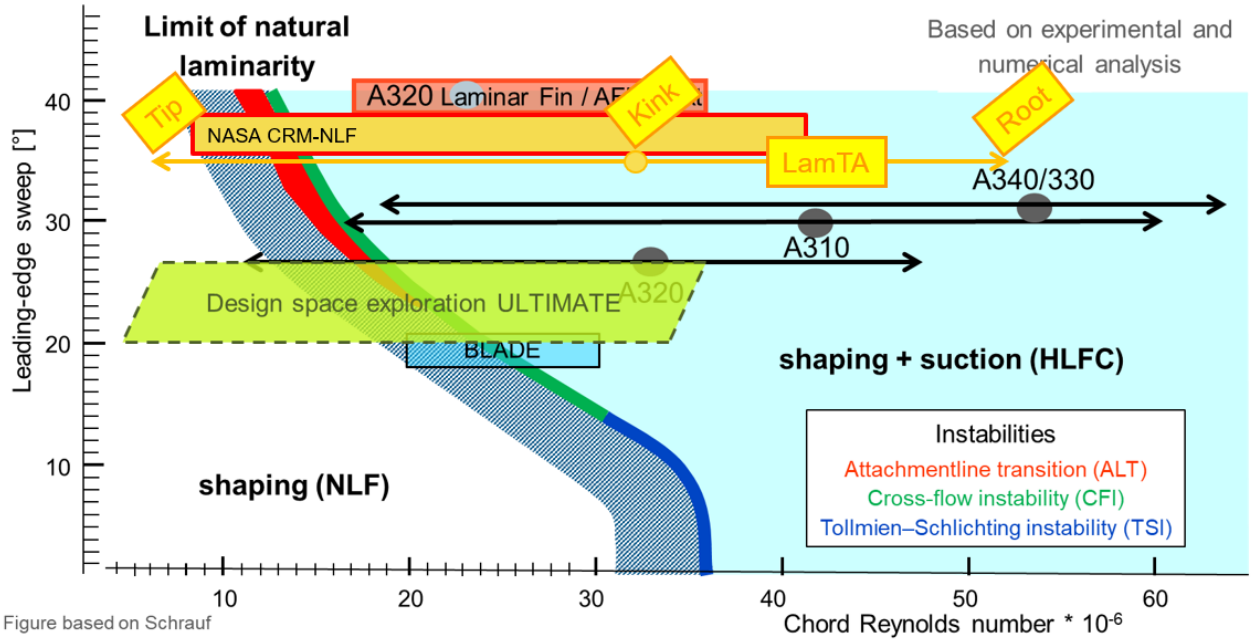


Figure 7 – Reynolds number and sweep range of laminar flow tests, based on [16]

Figure 6a shows how the pressure distributions have been modified to accommodate an stronger CATNLF gradient at an η positions of 0.66 and fig. 6b shows the impact on the Nts Ncf curve. Previously, without HLFC, transition was taking place at an x/c of 3.2 %, now, The Ncf factors are being dampened up to a minimum value 2 which allows for a lon steady gradient and lead to a transition at an x/c of 43.5 %. Furthermore at this position Re_θ has been reduced from value 135.7 to 98.7

Further work is required to asses how much can be achieved though CATNLF and if there is some trade-off at the LamTA configuration regarding $C_{L\ MAX}$ and available space for high lift devices.

6. Conclusion

During the LamTA project the usage of CATNLF Profiles has been further expanded from the previous project HLFC-WIN, both the NLF and the HLFC laminar extents have increased, which together with the aspect ratio increase lead to a geometry with a very good performance. The drag reduction achieved through laminarization is 19 d.c, which will be further developed to achieve the 26 d.c. reduction achieved by NASA CRM-NLF.

There is still much work to be done, and the CATNLF design strategy has still potential to further improve the NLF geometry and reduce the need of HLFC on long distance aircraft.

7. Contact Author Email Address

Javier.RuberteBailo@dlr.de,

8. Copyright Statement

The authors confirm that they, and/or their company or organization, hold copyright on all of the original material included in this paper. The authors also confirm that they have obtained permission, from the copyright holder of any third party material included in this paper, to publish it as part of their paper. The authors confirm that they give permission, or have obtained permission from the copyright holder of this paper, for the publication and distribution of this paper as part of the ICAS proceedings or as individual off-prints from the proceedings.

References

[1] Streit T, Ruberte Bailo J, Büscher A, and Seitz A. Design of a highly efficient transport nlf aircraft with a backward swept wing and a long single-aisle fuselage. In *34th Congress of the International Council of the Aeronautical Sciences, ICAS*, 2024.

[2] Streit T, Kruse M, Kilian T, Geyr J V, and Petropoulos I. Aerodynamic design and analysis of HLFC wings within the European project HLFC-WIN. In *ICAS 2022: 33rd Congress of the International Council of the Aeronautical Sciences*, 2022.

[3] Campbell R L and Lynde M N. Natural laminar flow design for wings with moderate sweep. In *34th AIAA Applied Aerodynamics Conference*, page 4326, 2016.

[4] Lynde M N, Campbell R L, and Viken S A. Additional findings from the common research model natural laminar flow wind tunnel test. In *AIAA Aviation 2019 Forum*, page 3292, 2019.

[5] Tokugawa N, Ishida T, Ueshima K, and K Ohira. Experimental validation of natural laminar fin at flight reynolds number. *Journal of Aircraft*, pages 1–4, 2025.

[6] Streit T and Hoffrogge C. DLR transonic inverse design code, extensions and modifications to increase versatility and robustness. *The Aeronautical Journal*, 121(1245):1733–1757, 2017.

[7] Streit T, Wedler S, and Kruse M. DLR natural and hybrid transonic laminar wing design incorporating new methodologies. *The Aeronautical Journal*, 119(1221):1303–1326, 2015.

[8] Schrauf G. Lilo 2.1 user's guide and tutorial. *GSSC Technical Report*, 6, 2006.

[9] Schwamborn D, Gerhold T, and Heinrich R. The DLR TAU-code: recent applications in research and industry. 2006.

[10] Wunderlich T and Dähne S. Multidisciplinary optimization of load adaptive wings for highly efficient long-haul airliners. In *The 9th European Congress on Computational Methods in Applied Sciences and Engineering, ECCOMAS Congress*, 2024.

[11] Fröhler B, Martinek P, Häßy J, Wunderlich T, Hepperle M, and Kilian T. Aerodynamic advances through laminar flow: A conceptual aircraft design study. 2025.

[12] Schulze M and Ruberte Bailo J. The effect of laminar compared to turbulent airfoils on the aeroelastic assessment of a long-range transport aircraft configuration. In *DLRK*, 2025.

[13] Vassberg J, Dehaan M, Rivers M, and Wahls R. Development of a common research model for applied cfd validation studies. In *26th AIAA applied aerodynamics conference*, page 6919, 2008.

[14] Lynde M N and Campbell R L. Computational design and analysis of a transonic natural laminar flow wing for a wind tunnel model. In *35th AIAA Applied Aerodynamics Conference*, page 3058, 2017.

[15] Sebastian Helm, Michael Fehrs, Normann Krimmelbein, and Andreas Krumbein. Transition prediction and analysis of the crm-nlf wing with the dlr tau code. In *STAB/DGLR Symposium*, pages 185–194. Springer, 2020.

[16] Schrauf G. Status and perspectives of laminar flow. *The aeronautical journal*, 109(1102):639–644, 2005.

[17] Thomas S Streit, Arne Seitz, Stefan Hein, and Philipp Kunze. Nlf potential of laminar transonic long range aircraft. In *AIAA Aviation 2020 Forum*, page 2748, 2020.